2-2-5 Application of the Magnetospheric Model for Numerical Forecast – Validation Using the *AE* Index –

KITAMURA Kentarou, SHIMAZU Hironori, FUJITA Shigeru, WATARI Shinichi, KUNITAKE Manabu, SHINAGAWA Hiroyuki, and TANAKA Takashi

Real-time magnetohydrodynamic (MHD) simulation of the solar solarwind-magnetosphere-ionosphere (S-M-I) coupling system was used to calculate auroral electrojet (AE) indices. We compared the simulated *AE* indices for 247 days with the *AE* indices deduced from the magnetic variations at up to 12 stations located around the auroral latitude. The results show that the simulated *AE* reproduces the observed *AE* indices well. Of the 247 days, 64% had crosscorrelation coefficients of more than 0.5. The result of the analysis indicates that the prediction of the *AE* index could be one of the most realistic contests in the space weather forecast. In this paper, the implication of the solarwind-magnetosphere coupling which is deduced from the comparison analysis between the onserved and simulated *AE* indices is also discussed.

Keywords
Real-time MHD simulation, *AE* index, Substorm

1 Introduction

Among the great volume of space environment information used for space weather forecasts, the *AE* (Auroral Electrojet) index—calculated based on data from geomagnetic observations on the ground—is widely used for indicating auroral activity in the polar regions. Auroral activity is known to involve drastic brightening caused by such phenomena as substorms in the magnetosphere due to solar wind disturbances. In a brightening event, a three-dimensional current system is formed between the magnetosphere and ionosphere, causing a sudden and intense electrojet flow in the polar ionosphere. The electrojet in the ionosphere (as reflected in the *AE* index) causes geomagnetic variations on the ground. Therefore, the *AE* index is very useful in solar-terrestrial physics for surveying the space environment, as it contains diverse information as a result of solar wind-magnetosphere-ionosphere coupling.

The National Institute of Information and Communications Technology (NICT) calculates plasma and magnetic field fluctuations in the solar wind, magnetosphere and ionosphere in real time through magnetohydrodynamic (MHD) simulation using a supercomputer (SX-8). For the upstream boundary conditions, this simulation uses real-time information on the solar wind magnetic field (observed by the ACE) and solar wind plasma. The ACE monitors solar wind at the L1 point about 220 Re (Re: radius of the earth) upstream from the earth toward the sun[1], and NICT receives observational data in real time with its 10-m antenna. Since it takes solar wind about an hour to propagate from the Advanced Composition Explorer (ACE) to reach the earth, magnetospheric fluctuations provided by this simulation can be used for space weather forecasts in predicting magnetospheric disturbances to be experienced one hour later.

2 *AE* Index

The *AE* index is prepared based on geomagnetic data observed at 12 observation points that are basically evenly distributed in the longitudinal direction in the auroral zone [2] [3]. These observations and data transfer are currently conducted based on an international partnership centered on the RapidMag project with participants from the following organizations: NICT; WDC, and Kyoto University; the Arctic and Antarctic Research Institute (AARI); the Institute for Dynamics of Geospheres (IDG), Russian Academy of Sciences; the Geophysical Institute (GI), University of Alaska; and the Johns Hopkins University Applied Physics Laboratory (JHU/APL) [4]. Table 1 lists the geomagnetic observatories used for calculating the *AE* indices. The effects of auroral electrojet contribute significantly to magnetic field fluctuations at these observatories whose locations are distributed at geomagnetic latitudes of 60 to 70 degrees.

The north-south component (H) of geomagnetic variations acquired at these observation points is used to calculate the *AE* indices. Figure 1 shows a diagram superposed with the H component at each observation point on November 8, 2005, after being baseline-compensated. The data obtained at seven observation points on that day were usable. The maximum envelope of superposed plots is shown in red; the minimum envelope is shown in blue. The electrojet in the east-west direction above the ionosphere contributes most to fluctuations of the geomagnetic H component in the auroral zone. In other words, the eastward electrojet causes positive (northward) fluctuations of the H component, while the westward electrojet causes negative (southward) magnetic field fluctuations. In Fig. 1, the red plots indicating the eastward electrojet are the *AU* indices; the blue plots indicating westward current are the *AL* indices.

As shown in Fig. 1, the red *AU* indices sharply increase from around 05:40 UT and then the blue *AL* indices sharply decrease from

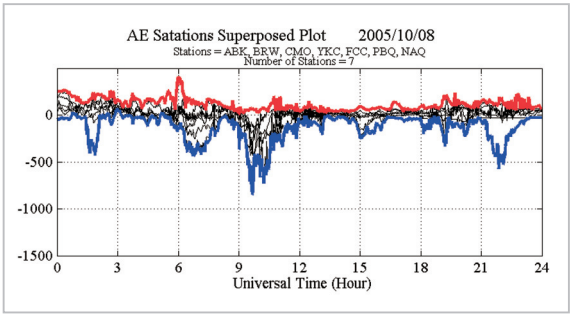

Fig. 1 *Superposed plots at AE observation points on October 8, 2005 (geomagnetic H component)*

Table 1 *List of observation points used for the AE index (excerpt from the WDC website, Kyoto University)*

Observatory	Station Code	Geographic Coord.		Geomagnetic Coord.	
		Lat.(°N)	Long.(°E)	Lat.(°N)	Long.(°E)
Abisko	ABK	68.36	18.82	66.04	115.08
Dixon Island	DIK	73.55	80.57	63.02	161.57
Cape Chelyuskin	CCS	77.72	104.28	66.26	176.46
Tixie Bay	TIK	71.58	129.00	60.44	191.41
Cape Wellen	CWE	66.17	190.17	61.79	237.10
Barrow	BRW	71.30	203.25	68.54	241.15
College	CMO	64.87	212.17	64.63	256.52
Yellowknife	YKC	62.40	245.60	69.00	292.80
Fort Churchill	FCC	58.80	265.90	68.70	322.77
Poste-de-la-Baleine	PBQ	55.27	282.22	66.58	347.36
Narsarsuaq (Narssarssuaq)	NAQ	61.20	314.16	71.21	36.79
Leirvogur	LRV	64.18	338.30	70.22	71.04

around 06:20 UT. The eastward ionospheric current is dominant during the period of increases in the *AU* indices, thereby indicating higher magnetospheric convection related to the growth phase of substorms in the magnetosphere. Then, with the onset of the substorm expansion phase, the westward electrojet is sharply reduced. In this manner, the *AU* and *AL* indices represent the longitudinal maximum electrojet in the eastward and westward directions, respectively. In addition, the *AE* and *AO* indices are calculated from the *AU* and *AL* indices as shown in the equations below [2][3].

$$AE = AU - AL$$
$$AO = (AU + AL)/2$$

The *AE* indices calculated above strongly reflect fluctuations of the ionospheric electrojet in conjunction with a developing aurora. Developing auroral electrojet resulting from substorms can also be read at 09:00 and 21:00 UT after 06:20 UT in Fig. 1. Since electrojet fluctuations due to auroral activity appear as a result of the solar wind-magnetosphere-ionosphere coupling process, such fluctuations are considered to reflect the physical process in each coupling.

3 Real-Time Simulation

Past studies have shown that MHD simulation well reproduces magnetospheric disturbances including substorms [5]-[12]. By using the solar wind data received from the ACE as upstream boundary conditions, NICT operates in real time the magnetospheric MHD simulator developed by Tanak [13]-[15]. The finite volume TVD (total variation-diminishing) method is used for simulation codes, where a grid system of unstructured grids is employed in order to efficiently resolve the couplings in differently scaled space such as the magnetosphere or ionosphere. The inner boundary of the simulation is set to a distance of 3 Re, where the electric field potential is projected on the ionosphere along the dipole magnetic field. The Pedersen and Hall currents are calculated with respect to the electric field potential that intrudes into the ionosphere according to Ohm's law in the ionosphere. The three-dimensional current system is calculated as follows:

$$\nabla \cdot \boldsymbol{\sigma} \nabla \Phi_I = G_m \left(rot \mathbf{B}_1 \cdot \mathbf{n}_b \right) = J_{\parallel}$$
$$\boldsymbol{\sigma} = \boldsymbol{\sigma}_{EUV} + k_1 \boldsymbol{\sigma}_{Diff} \left(P, \rho \right) + k_2 \boldsymbol{\sigma}_J \left(J_{\parallel} \right)$$
$$\Phi_m = \Phi_I - k_3 f_1 \left(J_{\parallel} \right) \left| J_{\parallel} \right|$$

where, σ denotes the electrical conductance tensor in the ionosphere, Φ_I the electric field potential in the ionosphere, Φ_m the magnetospheric potential at 3 Re, $\mathbf{B}_1$ the fluctuation component of the magnetic field, $\mathbf{n}_b$ the outward unit vector, and $J_{\parallel}$ the current component parallel to the magnetic lines (field aligned current). In addition, G_m is a geometric element for mapping from 3 Re to 1 Re. The ionospheric current can be determined by the electric field potential projected on the ionosphere, where electrical conductance is dynamically calculated in MHD simulation, but not provided by a model. The terms σ_{EUV}, σ_{Diff}, and σ_J represent the electrical conductance due to solar ultraviolet radiation, electrical conductance due to the transfer particles of diffuse aurora, and electrical conductance due to the transfer particles of field aligned current, respectively. The term σ_{Diff} is defined as a function of solar wind dynamic pressure (P) and solar wind density (ρ), and f_1 is a coefficient to determine the direction of the field aligned current. The terms k_1 to k_3 are scaling coefficients. Electrical conductance (η) is defined as follows:

$$\eta = k_4 f_2 \left(x \right) \left| J \right|^2 / \left| B \right|^2$$

where, the term f_2 as a function independent to time monotonically increases from the domain close to the earth ($x > -20$ Re) and saturates in the domain away from the earth ($x > -60$ Re). In addition, k_4 is a coefficient for scaling.

Figure 2 shows conditions of the magnetosphere and polar ionosphere as reproduced in real-time simulation for the clock time (see the diagram at the lower right in the figure) after

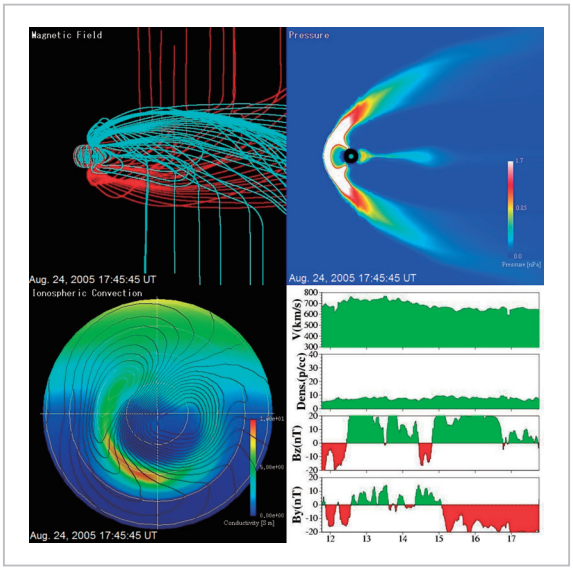

Fig.2 *Example of MHD simulation*

(Upper left: distribution of the magnetic field; upper right: distribution of pressure; lower left: distribution of electrical conductance and electric field potential in the polar cap region; lower right: input solar wind parameter)

interplanetary shock waves collide with the magnetosphere. The picture at the upper right illustrates the distribution of plasma pressure on the meridian plane. The conditions reproduced due to shock wave collision are the increased pressure in the sheath domain in front of the magnetosphere and a thinned plasma sheet in its tail, as well as the ejection of plasmoid. In addition, the picture at the lower left indicates the electric field potential of the ionosphere as viewed from the North Pole (contour plot) and the electrical conductance (color map), where a good reproduction of the following conditions are understood: increased electrical conductance due to the transfer of auroral particles in the domain before midnight directly after shock wave collision, and the electric field developing in the dawn-dusk direction.

4 Comparison of Simulated and Observed *AE* Indices

4.1 Differences in *AE* index due to simulated calculation method

Geomagnetic fluctuations on the ground can be simply determined by the Biot-Savart law based on the ionospheric current system obtained from the simulation. As previously described, an *AE* index is calculated from geomagnetic fluctuations observed at a total of 12 observation points located in the auroral zone, giving a maximum variation of about 11 degrees latitude relative to the location of these observation points. We thus used two different methods for trial calculation of the *AE* index in the simulation as follows: (1) *AE* index calculated from geomagnetic fluctuations at the grid point closest to the original observation point (hereinafter notated as AE_{12}), and (2) *AE* index calculated from magnetic field fluctuations at all grid points located between 60 to 70 degrees latitude (hereinafter notated as AE_{all}). (The same notation system also applies to the *AL*, *AU* and *AO* indices.)

Figure 3 (a) shows the *AE*, *AU*, *AL* and *AO* indices on July 28, 2006. Each index is shown in superposition of the indices determined by observation (blue line), AE_{12} (black line), and AE_{all} (red line). For the observed *AE* index, we used the Quick-Look (QL) *AE* index provided by the World Data Center (WDC) for Geomagnetism, Kyoto University (http://wdc.kugi.kyoto-u.ac.jp/aeasy/index-j.html). The QL data is disclosed for the quasi-real-time provision of data without minor errors being corrected. Therefore, the data may not be intrinsically suited for analytical use. However, we used the real-time or QL data for both the ACE and the *AE* indices, since our study intends to verify the applicability of such real-time data to space weather forecasts.

As shown in Fig. 3 (a), there is a significant increase in each index due to substorms that occurred from 02:00 to 06:00 UT. Regarding the *AE* index, simulated and observed *AE* indices are well consistent one another as a whole; however, in terms of magnitude, AE_{all} tends to be calculated larger than AE_{12}. The reason for this tendency is considered to be the location of two of the 12 observation points at a magnetic longitude of more than 70 degrees. In particular, the observation point on the high longitude dusk side is considered to contribute

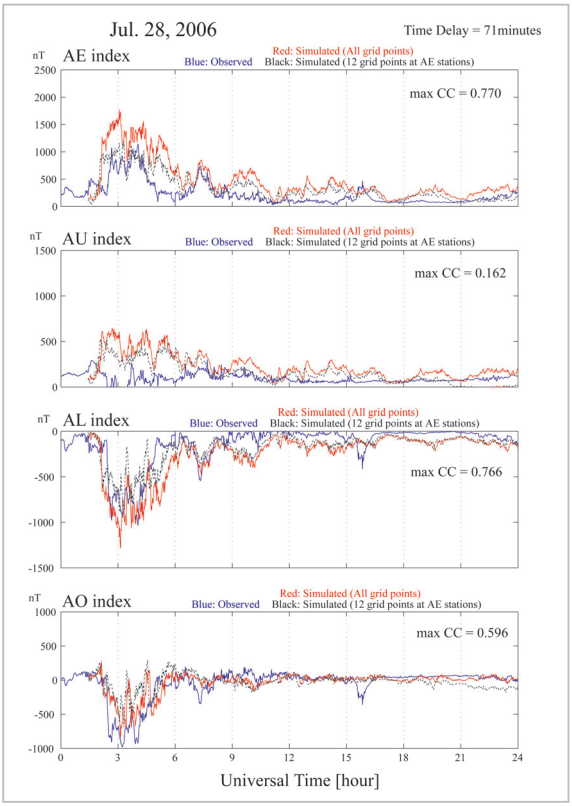

Fig.3 (a) *Comparison of observed and simulated indices (example of July 28, 2006)*

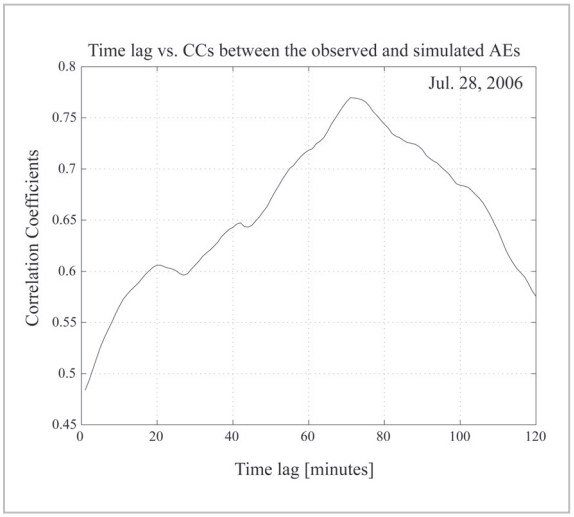

Fig.3 (b) *Relation of the time difference and cross-correlation coefficient between observation and simulation*

to this tendency with the *AU* index [16]. Since the difference between AE_{all} and AE_{12} is still sufficiently fractional compared with the difference between AE_{all} and the observed *AE* index, we handled AE_{all} as the *AE* index determined from the simulation.

4.2 Reproducibility of the *AE* index in the simulation

The reproducibility of the *AE* index determined by the simulation is verified in this section by using the example of Fig. 3 (a). For the observed *AE* index, clear auroral activity with a maximum magnitude exceeding 1000 nT is recognized in the period from 02:00 to 05:00 UT. For the simulated *AE* index, similar activity is also found in the same period, but with magnitude just over 1700 nT overlapping with an inter-peak magnitude of fluctuation as large as about 700 nT (not found for the observed *AE* index) in the same time period. The auroral activity from 06:00 to 08:00 UT is very much consistent between the observed and simulated *AE* indices.

In the figure, the calculation results of cross-correlation coefficients of the observed and simulated indices are shown for each of the *AU*, *AL* and *AO* indices. The cross-correlation coefficients for the *AL* and *AO* indices are high at 0.766 and 0.596, respectively, indicating a high correlation, while that for the *AU* index at 0.162 indicates practically no correlation. This can also be verified from significant fluctuations in observation (blue) and simulation (red and black) during the period from 02:00 to 05:00 UT in the *AU* index plots. During a disturbed period, the simulated *AU* index is much larger than the observed *AU* index. The variance reaches a maximum as large as 500 nT.

These results suggest that the global MHD simulation used in this study estimates the eastward electrojet contributing to the *AU* index as being larger than it actually was during such disturbances as substorms, although the simulation well reproduces the westward auroral electrojet contributing to the *AL* index. This section only introduced one typical example of a substorm event, but a similar tendency was found in many other events. The reason will be discussed later based on statistical

results.

4.3 Time variance between observed and simulated indices

Figure 3 (b) shows the calculation results of cross-correlation coefficients for the observed and simulated *AE* indices provided in Fig. 3 (a). The horizontal axis represents the time variance; the cross-correlation coefficients appear to vary according to the quadratic function with respect to time variance. The maximum cross-correlation coefficient (maxCC) was 0.77 at a time variance of 71 minutes. This time variance is equivalent to the propagation time from the ACE to the earth at a solar wind velocity of about 330 km/s.

The time variance between the observed and simulated *AE* indices is an important element for evaluating the *AE* index as determined by the simulation. The time variance should decrease with higher solar wind velocity, since it primarily results from the velocity of solar wind propagation from the ACE as previously described. Figure 4 illustrates the relation between the time variance and solar wind velocity. The horizontal axis represents the time variance; the vertical axis represents $1/V$ (V = solar wind velocity). Only events with maxCC of 0.4 or more are plotted in the figure.

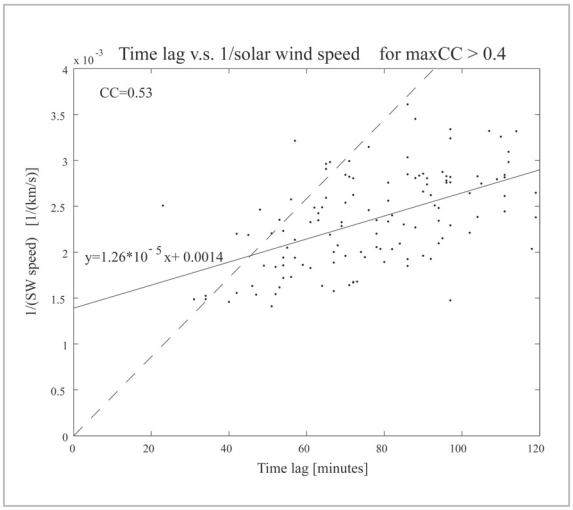

Fig.4 *Relation between time variance and solar wind velocity for observation and simulation (events with maximum cross-correlation coefficient (maxCC) of 4 or larger)*

The $1/V$ value is found to increase with a larger time variance despite the well-dispersed plots. The cross-correlation coefficient between the two elements in these plots was 0.53. Linear regression analysis of the dispersed plots revealed the following: $y = 1.26 \times 10^{-5}x + 1.40 \times 10^{-3}$ (x: time variance; y: $1/V$). This result suggests that the time variance mainly indicates the dependence on solar wind velocity, while the y-intercept of 1.40×10^{-3} implies that the time variance may also be controlled by a factor other than solar wind velocity.

The broken line in Fig. 4 indicates the relation of the predicted 1/V with time variance under an assumed ACE location at a distance of 220 Re from the earth toward the sun. Based on this relation, the actual time variance is understood to be larger than the predicted time variance for almost all events. This also supports the idea that solar wind propagation time is not the only determinant of time variance between the observed and simulated *AE* indices. Moreover, the time constant for the response to solar wind variation in the magnetosphere is shown to significantly contribute to deviation from the predicted value. The findings above may also coexist with another effect that could alter the structure of solar wind during its propagation from the ACE to the magnetosphere [17]–[20].

4.4 Distribution of the cross-correlation coefficients

Figure 5 indicates the frequency distribution of maxCC for the *AE*, *AL*, *AU* and *AO* indices covering 247 days from August 2005 through September 2006, excluding the days of missed solar wind measurements or computer downtime. Here, maxCC for the *AE* index is mainly distributed in the range from 0.4 to 0.8, with 0.5 or more indicated on 158 days, or 64% of the total number of days. This result also indicates that the simulated *AE* index accurately reproduces actual auroral activity and is therefore usable for forecasts an hour ahead. In Fig. 5, (b) to (d) indicate the frequency distribution of maxCCs for the *AU*, *AL* and *AO* indices, respectively. The distribution of

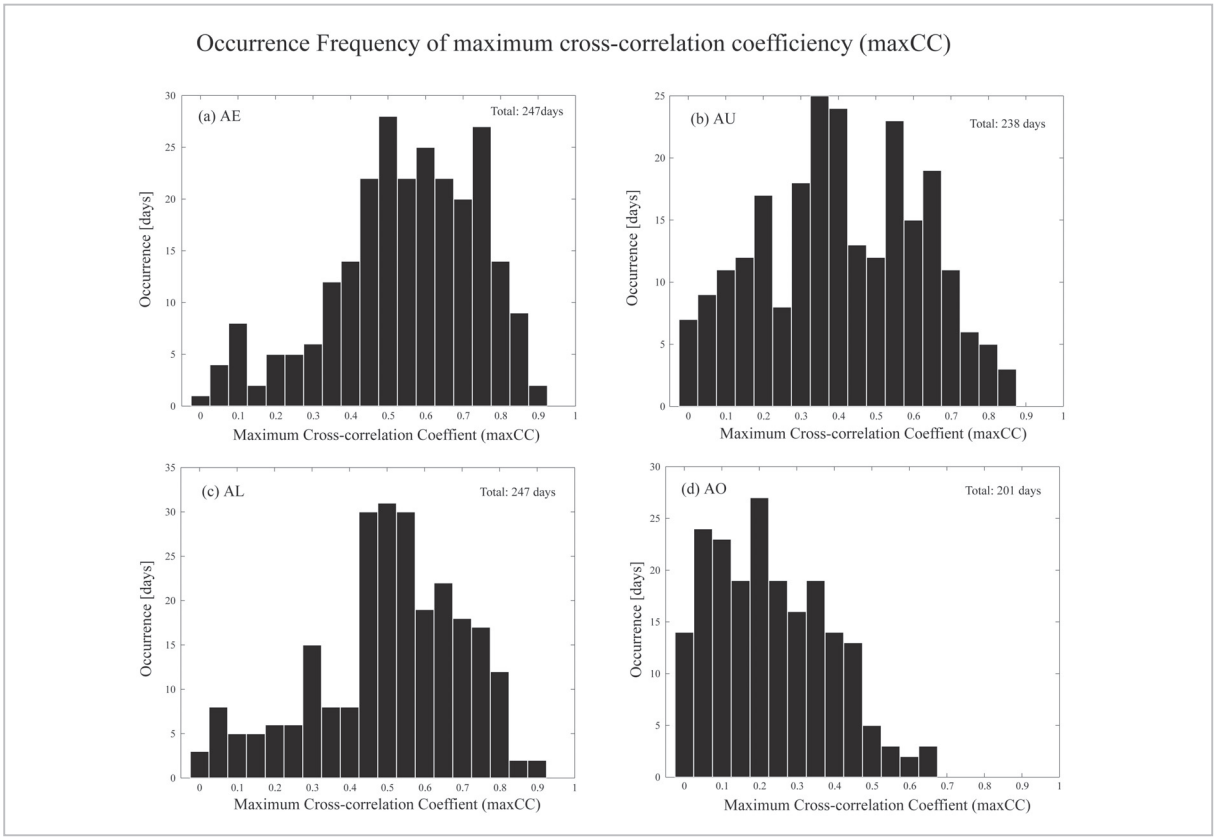

Fig.5 *Frequency distribution of maxCC for each index*

the *AL* index shows a tendency similar to the *AE* index, where maxCC of 0.5 or more accounts for about 54% of the total number of days. Conversely, the *AU* and *AO* indices indicate different frequency distributions. The *AU* index shows a widely spread distribution with the peak at 0.4. The *AO* index was found to afford very bad reproducibility, 96% of which showed below 0.5 with the peak of 0.2.

The difference between the *AL* and *AU* indices is considered the variance in ionospheric current reproducibility. This simulation well reproduces the accidental westward electrojet caused by substorms as confirmed by the high maxCC of the *AL* index. Unlike the westward current, the eastward current is not believed to flow concentrated in a narrow area during the substorm expansion phase [21][22]. The electric field potential in the polar regions during a substorm is known to be smaller in the cell on the dusk side, and the *AU* index is a function of the electric field potential of the polar cap [23]. Based on these considerations, our simulation is not intended to accurately reproduce weak eastward electrojet distributed in a wide area. Therefore, the magnetosphere-ionosphere coupling (not incorporated in this simulation model) must be carefully considered.

4.5 Evaluation of the simulated *AE* index during disturbances

From the perspective of *AE* index forecasting, evaluating the reproducibility of the simulated *AE* index should be focused on a disturbed period when the *AE* index shows large variation, rather than a quiet period. We thus compared maxCC with standard deviation for the *AE* index (one-minute sampling) as determined from observation. In Fig. 6, the horizontal axis represents standard deviation of the observed *AE* index and the vertical axis represents maxCC. The plots are widely dispersed with no linear relation being clearly observed. However, distribution trends in the domains of deviation larger than 100 nT are somewhat dif-

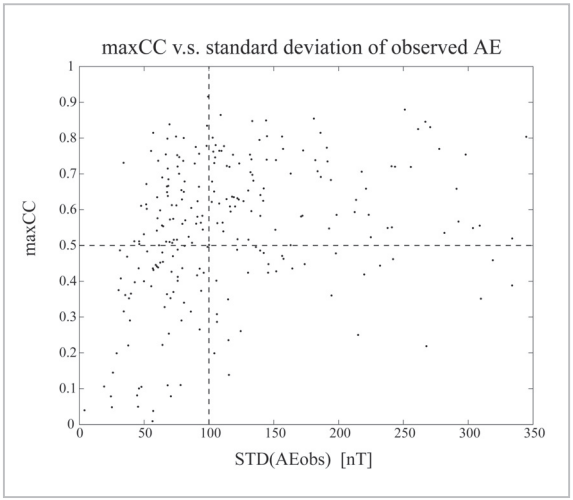

Fig.6 *Relation between standard deviation and maxCC of the observed AE index*

ferent. Focusing on the domain of standard deviation of 100 nT or larger (corresponding to the *AE* disturbance period), 74% of the total 120 days showed maxCC of 0.5 or more. In contrast, the domain of standard deviation of 100 nT or smaller only accounted for 36% of the total days, with maxCC of 0.5 or more. In other words, reproducibility of the simulated *AE* index is apparently superior in a disturbed period with drastic fluctuations than in a quiet period.

The time step of a simulation is generally determined according to the CFL (Courant-Friedrichs-Lewy) condition, or typically a second or less. Although our simulation for the simulated *AE* index produced data from one-minute sampling, short frequency fluctuations may occur in the simulation. Tanaka [24] well reproduced observational characteristics from the growth to expansion phases of substorms by using MHD simulation conducted under ideal solar wind conditions where magnetospheric convection was sufficiently developed. Since these MHD simulations used solar wind data observed in real time by the satellite, the fractional perturbation components of solar wind during the quiet period are considered greatly reflected in the simulations.

5 Solar wind-magnetosphere coupling system considered from the simulated *AE* index

Broadly used as an index for auroral activity, the *AE* index is particularly utilized more often than not for determining substorms and recognizing the characteristics thereof. A substorm is a typical phenomenon of the solar wind-magnetosphere coupling system, and fluctuations of the *AE* index are well known to highly depend on the parameters (e.g., magnetic field, velocity, pressure) of solar wind upstream from the substorm. However, many questions about the accumulation and release of energy when substorms occur remain unanswered [24]–[30].

Many comparative studies have been conducted on *AE* index fluctuations due to solar wind disturbances (see [31], [32] and [16]). These studies suggest that the solar wind-magnetosphere coupling system is essentially nonlinear, and that *AE* index fluctuations include the process of accumulating and releasing energy in substorms.

The most notable differences between the simulated and observed *AE* indices described in this paper are that many short frequency fluctuations of large magnitude overlap during *AE* index disturbances, and small-scaled short frequency fluctuations and substorm-like variances appear in the simulated *AE* indices even during a quiet period. With various time constant variations included in actual solar wind fluctuations, this simulation with inputs of real-time solar wind data calculates all magnetospheric responses up to minor fluctuations. Uritsky [33] pointed out that solar wind fluctuations within 3.5 hours are not fundamentally related to the time constant for variation in *AE* index intensity. The inconsistency between the simulated and observed *AE* indices in our simulation differs from such actual magnetospheric response. That is, our findings suggest that a process of buffering or rectifying the inflow of energy, which is not included in this simulation, may be included in magnetospheric response to the fractional, short frequency fluc-

tuations of solar wind in the actual solar wind-magnetosphere coupling system.

6 Summary

The *AE* index derived from this MHD simulation showed good consistency with the observed *AE* index, indicating a particularly high correlation during magnetospheric disturbances. This result demonstrated that an *AE* index forecast based on MHD simulation is fully possible. In order to conduct a virtually real forecast with better accuracy in the future, discussions are required on the introduction of the particle effect and how to incorporate the explosive/accidental phenomena in a short period into simulation rather than the calculative time step.

Acknowledgments

To prepare this paper, we used *AE* index data from the database of the World Data Center for Geomagnetism at Kyoto University. The Space Environment Center (SEC) of the National Oceanic and Atmospheric Administration (NOAA) provided the solar wind data. We wish to thank all parties concerned for their valuable assistance.

References

1 R. D. Zwickl, K. A. Doggett, S. Sahm, W. P. Barrett, R. N. Grubb, T. R. Detman, V. J. Raben, C. W. Smith, P. Riley, R. E. Gold, R. A. Mewaldt, and T. Maruyama, "The NOAA Real-Time Solar-Wind (RTSW) system using ACE data," Space Sci. Rev., 86, 633–648, 1998.

2 T. N. Davis and M. Sugiura, "Auroral electrojet activity index AE and its universal time variations," J. Geophys. Res., 71, 785, 1966.

3 T. Kamei, M. Sugiura, and T. Araki, "Auroral electrojet (AE) indices for January-June 1978," Data book No. 3, World Data Center for Geomagnetism, Kyoto University, Japan, 1981

4 K. Takahashi, C. Meng, T. Kamei, T. Kikuchi, and M. Kunitake, "Near-Real-Time Auroral Electrojet Index: An International Collaboration Makes Rapid Delivery of Auroral Electrojet Index," Space Weather, 2, S11003, doi: 10.1029/2004SW000116, 2004.

5 R. J. Walker, T. Ogino, J. Raeder, and M. Ashour-Abdalla, "A global magnetohydrodynamic simulation of the magnetosphere when the interplanetary magnetic field is southward: The onset of magnetotail reconnection," J. Geophys. Res., 98, 17235, 1993.

6 J. A. Fedder and J. G. Lyon, "The Earth's magnetosphere is 165 RE long: Self-consistent currents, convection, magnetospheric structure, and processes for northward interplanetary magnetic field," J. Geophys. Res., 100, 3623, 1995.

7 J. R. Raeder, J. Walker, and M. Ashour-Abdalla, "The structure of the distant geomagnetic tail during long periods of northward IMF," Geophys. Res. Lett., 22, 349–352, 1995.

8 D. S. Spicer, S. T. Zalesak, R. Lohner, and S. Curtis, "Simulation of the magnetosphere with a new three dimensional MHD code and adaptive mesh refinement: Preliminary results," Adv. Space Res., 18, 253, 1996.

9 R. K. Elsen and R. M. Winglee, "The average shape of the Magnetopause: A comparison of three-dimensional global MHD and empirical models," J. Geophys. Res., 102, 4799–4820, 1997.

10 P. H. Janhunen and E. J. Koskinen, "The closure of Region-1 field-aligned current in MHD simulation," Geophys. Res. Lett., 24, 1419–1422, 1997.

11 W. W. White, G. L. Siscoe, G. M. Erickson, Z. Kaymaz, N. C. Maynard, K. D. Siebert, B. U. O. Sonnerup, and D. R. Weimer, "The magnetospheric sash and the cross-tail S," Geophys. Res. Lett., 25, 1605, 1998.

12 P. Song, D. L. De Zeeuw, T. I. Gombosi, C. P. T. Groth, and K. G. Powell, "Numerical study of solar wind - magnetosphere interaction for northward interplanetary magnetic field," J. Geophys. Res., 104, 28361, 1999.
13 T. Tanaka, "Finite volume TVD scheme on an unstructured grid system for three-dimensional MHD simulation of inhomogeneous systems including strong background potential fields," J. Comput. Phys., 111, 381–389, 1994.
14 T. Tanaka, "Generation mechanisms for magnetosphere-ionosphere current systems deduced from a three-dimensional MHD simulation of the solar wind-magnetosphere-ionosphere coupling processes," J. Geophys. Res., 100, 12057, 1995
15 T. Tanaka, "Interplanetary magnetic field By and auroral conductance effects on high-latitude ionospheric convection patterns," J. Geophys. Res., 106, 24505, 2001
16 J. H. Allen and H. W. Kroehl, "Spatial and temporal distributions of magnetic effects of auroral electrojets as derived from AE indices," J. Geophys. Res., 80, 3667–3677, 1975.
17 K. I. Paularena, G. N. Zastenker, A. J. Lazarus, and P. A. Dalin, "Solar wind plasma correlations between IMP 8, INTERBALL-1 and WIND," J. Geophys. Res., 103, 14601, 1998
18 J. D.Richardson, F. D. Dashevskiy, and K. I. Paularena, "Solar wind plasma correlations between L1 and Earth," J. Geophys. Res., 103, 14619, 1998
19 J. P. Eastwood, A. Balogh, and M. W. Dunlop, "Cluster observations of the heliospheric current sheet and an associated magnetic flux rope and comparisons with ACE," J. Geophys. Res., 107, 1365, doi: 10.1029/2001JA009158, 2002
20 R. P. Lepping, C. –C. Wu, and K. McClernan, "Two-dimensional curvature of large angle interplanetary MHD discontinuity surfaces: IMP-8 and WIND observations," J. Geophys. Res., 108, 1279, doi: 10.1029/2002JA009640, 2003
21 Y. Kamide, A. D. Richmond, B. A. Emery, C. F. Hutchins, B. –H. Ahn, O. de la Beaujardiere, J. C. Foster, R. A. Heelis, H. W. Kroehl, F. J. Rich, and J. A. Slavin, "Ground-based studies of ionospheric convection associated with substorm expansion," J. Geophys. Res., 99, 19451, 1994.
22 Y. Kamide, W. Sun, and S. I. Akasofu, "The average ionospheric electrodynamics for the different substorm phases," J. Geophys. Res., 101, 99, 1996.
23 D. R. Weimer, "Substorm influence on the ionospheric electric potentials and currents," J. Geophys. Res., 104, 185, 1999.
24 T. Tanaka, "The state transition model o the substorm onset," J. Geophys. Res., 105, 21081, 2000.
25 D. N. Baker, A. J. Klimas, D. Vassiliadis, T. I. Pulkkinen, and R. L. McPherron, "Reexamination of driven and unloading aspects of magnetospheric substorms," J. Geophys. Res., 102, 7169, 1997.
26 Y. Shi, E. Zesta, L. R. Lyons, K. Yumoto, and K. Kitamura, "Statistical study of effect of solar wind dynamic pressure enhancements on dawn-to-dusk ring current asymmetry," J. Geophys. Res., 111, A10216, doi: 10.1029/2005JA011532, 2006.
27 K. Kitamura, H. Kawano, S. Ohtani, A. Yoshikawa, and K. Yumoto, "Local-time Distribution of Low and Middle Latitude Ground Magnetic Disturbances at Sawtooth Injections of April 18–19, 2002," J. Geophys. Res., 110, A07208, doi: 10.1029/2004JA010734, 2005.
28 K. Kitamura, H. Kawano, S. Ohtani, A. Yoshikawa, K. Yumoto, and the Circum-pan Pacific Magnetometer Network Group, "Quasi-periodic substorms during recovery phase of magnetic storm for space weather study," Proceedings of the International Symposium on Information Science and Electrical Engineering 2003, 354–357, Nov. 13–14, 2003.

29 L. R. Lyons, G. T. Blanchard, J. C. Samson, R. P. Lepping, T. Yamamoto, and T. Moretto, "Coordinated observations demonstrating external substorm triggering," J. Geophys. Res., 102, 27039, 1997.
30 L. R. Lyons, D. –Y. Lee, C. –P. Wang, and S. B. Mende, "Global auroral responses to abrupt solar wind changes: Dynamic pressure, substorm, and null events," J. Geophys. Res., 110, A08208, doi: 10.1029/2005JA011089, 2005.
31 L, F. Bargatze, D. N., Baker, R. L., McPherron, and E. W. Hones, "Magnetospheric impulse response for many levels of geomagnetic activity," J. Geophys. Res., 90, 6387, 1985.
32 A. J. Klimas, D. Vassiliadis, D. N. Baker, and D. A. Roberts, "The organized nonlinear dynamics of the magnetosphere," J. Geophys. Res., 101, 13089–13113, 1996.
33 V. M. Uritsky, A. J. Klimas, and D. Vassiliadis, "Comparative study of dynamical critical scaling in the auroral electrojet index versus solar wind fluctuations," Geophys. Res. Lett., 28, 3809–3812, 2001.

***KITAMURA Kentarou**, Dr. Sci.*
Associate Professor, Department of Mechanical and Electrical Engineering, Tokuyama National College of Technology
Solar-Terrestrial Physics, Space Weather

***SHIMAZU Hironori**, Dr. Sci.*
Senior Researcher, Space Environment Group, Applied Electromagnetic Research Center
Space Physics

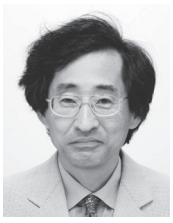

***FUJITA Shigeru**, Dr. Sci.*
Associate Professor, Meteorological College
Physics of the Magnetosphere-Ionosphere System

***WATARI Shinichi**, Dr. Sci.*
Research Manager, Space Environment Group, Applied Electromagnetic Research Center
Solar-Terrestrial Physics, Space Weather

KUNITAKE Manabu
Senior Researcher, Space Environment Group, Applied Electromagnetic Research Center
Magnetosphere Physics, Aeronomy

***SHINAGAWA Hiroyuki**, Ph.D.*
Senior Researcher, Space Environment Group, Applied Electromagnetic Research Center
Ionospheric Physics

***TANAKA Takashi**, Dr. Sci.*
Professor, Graduated School of Sciences, Kyushu University
Magnetospheric Compound System Physics